Journal of Catalysis 276 (2010) 16–23

Contents lists available at ScienceDirect

Journal of Catalysis

journal homepage: www.elsevier.com/locate/jcat

Determination of active site densities and mechanisms for soot combustion with O_2 on Fe-doped CeO_2 mixed oxides

Zhaoliang Zhang [a,*], Dong Han [a], Shaojie Wei [a], Yexin Zhang [a,b]

[a] College of Chemistry and Chemical Engineering, University of Jinan, 106 Jiwei Rd., Jinan 250022, China
[b] Liaoning Key Laboratory of Internal Combustion Engines, Institute of Internal Combustion Engine, Dalian University of Technology, 2 Linggong Rd., Dalian 116024, China

ARTICLE INFO

Article history:
Received 8 April 2010
Revised 3 August 2010
Accepted 18 August 2010
Available online 29 September 2010

Keywords:
Soot combustion
Active site
Ceria
Iron

ABSTRACT

Fe-doped CeO_2 mixed oxides were studied for soot combustion with O_2 under tight contact conditions. They show increased activity compared to that of pure CeO_2 and Fe_2O_3. The optimum Fe content according to soot ignition temperatures is Fe/(Ce + Fe) = 10 at.%. However, on the basis of turnover frequencies, the samples with a Fe/(Ce + Fe) ratio between 5 and 20 at.% show similar activity. Characterization of the catalysts and a kinetic study show that the reaction proceeds via a redox mechanism. The active sites were determined to be composed of Fe–O–Ce species, and the active oxygen was quantified using isothermal anaerobic titrations with soot as a probe molecule. The redox property for the Fe–O–Ce species is much stronger than for the Ce–O–Ce species. The methodology for quantifying active redox sites can be extended to soot combustion on all similar oxide systems.

1. Introduction

Ce oxides attract special attention for use in diesel soot combustion because of their oxygen storage capacity (OSC) [1,2]. The introduction of Fe into CeO_2 can improve the kinetic performance of soot combustion [3]. Additionally, RHODIA developed the last generation of fuel-borne catalysts (FBC) based on pure Fe colloidal particles with a high intrinsic oxidation property [4]. Reichert et al. [5] studied the reaction mechanism of soot combustion on Fe_2O_3. Among the CeO_2–Fe_2O_3 mixed oxides, Aneggi et al. [6] found that $Ce_{0.95}Fe_{0.05}O_2$ was the most active, while Yan et al. [7] reported that $Ce_{0.8}Fe_{0.2}O_2$ had the lowest ignition temperature and had a high thermal stability. Interestingly, CeO_2–Fe_2O_3 mixed oxides were also studied for CO (possible intermediate of soot combustion) oxidation. Bao et al. [8] and Singh and Hegde [9] respectively stated that $Ce_{0.9}Fe_{0.1}O_2$ and $Ce_{0.85}Fe_{0.15}O_2$ showed the best catalytic activity. Their work revealed that the CeO_2–Fe_2O_3 mixed oxides are very promising in catalyzing soot combustion, but no intrinsic activities based on turnover frequency (TOF) are given. Therefore, some results concerning the evaluation of the catalytic performance and the elucidation of the reaction mechanism seem to be inconsistent [6–9]. This is because the derived characteristic temperatures from the temperature-programmed oxidation (TPO) profiles, T_n (the temperature at which n% of the soot converts) and/or T_{max} (the temperature at which the maximum CO_x concentrations are observed), are not the reaction rate and cannot reveal much about the activity let alone the reaction mechanism. Recently, Gross et al. [2] observed the kinetic evidence related to the reaction mechanism for the K/CeO_2 catalyst, which suggests that kinetic experiments should not be omitted in the study of soot catalytic combustion [10].

TOF is defined as the ratio of the reaction rate to the active site density of the catalysts [11]. To calculate TOF values, the rate in the kinetic regime (internal and external mass and heat transfer are all excluded) must first be determined. The active sites should then be identified and accurately quantified, which is sometimes difficult for heterogeneous catalysis. Several cases of determination of the active sites and the TOF have been proposed in the literature. For supported metal catalysts, the metal sites are known to be active and the number can be obtained by H_2 [12] or CO [13] chemisorption. The acid sites [14] and base sites [15] on the catalyst are usually determined by NH_3 and CO_2 chemisorption, respectively. However, different strategies have been used for supported and bulk oxide catalysts. O_2 chemisorption after H_2 prereduction is a common approach, which involves reducing the catalyst surface with H_2 and then reoxidizing to determine the number of redox sites by the amount of O_2 adsorbed. This is not a very accurate method because (1) the actual reactant is not used as the probe molecule; (2) bulk reduction of the oxide can take place; (3) the reduction stoichiometry of the oxide is usually not known; and (4) both the prereduction step and the chemisorption step are highly sensitive to temperature. To solve these problems, a strategy for quantifying the number of active

* Corresponding author. Fax: +86 531 89736032.
E-mail address: chm_zhangzl@ujn.edu.cn (Z. Zhang).

0021-9517/$ - see front matter © 2010 Elsevier Inc. All rights reserved.
doi:10.1016/j.jcat.2010.08.017

sites by the chemisorption of the actual reactant has been reported [16]. However, this method is not suitable for solid–solid reactions such as soot combustion on oxide catalysts. In our latest work [17], we proposed that CO_2 chemisorption can be used to determine the density of active sites for soot combustion on potassium-supported Mg–Al mixed oxides. Recently, isothermal anaerobic titration at the reaction temperature with the actual reactant as the probe molecule has been shown to be an accurate technique for quantifying active redox site densities in metal oxide catalysts, in which all conditions are similar to those of actual reactions except for the presence of oxygen in the gas phase [18]. Because redox product formation is used for quantification, only active redox sites are counted. Polster et al. [19] successfully quantified the Cu–O–Ce redox sites for highly selective CO oxidation in H_2-rich atmospheres on Cu/CeO_2 catalysts using CO as the probe molecule. Inspired by these works, we quantified the active oxygen site densities and also the TOF for soot combustion on Fe-doped CeO_2 with variable Fe content. This is important for an accurate comparison of activity and for the elucidation of the reaction mechanism. This methodology for quantifying active redox site densities might be extended to soot combustion on all similar oxides that react through a redox process that includes lattice oxygen.

2. Experimental

2.1. Sample preparation

A series of Ce–Fe mixed oxides with 1, 5, 10, and 20 at.% Fe metal (Ce balance) were prepared by a coprecipitation method. Hereafter, they are denoted as x%Fe/y%CeO_2, in which x (=100Fe/(Fe + Ce)) and y (=100Ce/(Fe + Ce)) are the atom percentages of Fe and Ce, respectively. A stoichiometric solution (100 ml) of $Ce(NO_3)_3{\cdot}6H_2O$ and $Fe(NO_3)_3{\cdot}9H_2O$ was dropped into 150 ml of $NH_3{\cdot}H_2O$ solution (25%) under vigorous agitation, and the resultant precipitate was aged in air for a certain time at room temperature and pressure. The resultant precipitates were dried at 100 °C overnight and calcined at 650 °C for 6 h in static air. For comparison, pure Ce and Fe oxides were also prepared using a similar procedure, and these were determined to be CeO_2 and Fe_2O_3, respectively.

2.2. Characterization

X-ray powder diffraction (XRD) patterns were recorded on a Rigaku D/max-rc diffractometer employing Cu Kα radiation (λ = 1.5418 Å) operating at 60 kV and 40 mA. The details of the quantitative analysis are given in the Supplementary Information.

Field-emission scanning electron microscopy (FESEM) was conducted on a JEOL SU70. Transmission electron microscopy (TEM) with energy dispersive spectroscopy (EDS) was conducted on a JEOL JEM-2010 at an accelerating voltage of 200 kV.

The Brunauer–Emmett–Teller (BET) surface area and pore structure were measured by N_2 adsorption/desorption using a Micromeritics 2020 M instrument. Before N_2 physisorption, the sample was outgassed at 300 °C for 5 h.

X-ray photoelectron spectroscopy (XPS) data were obtained on an AXIS-Ultra instrument from Kratos Analytical using monochromatic Al Kα radiation (225 W, 15 mA, 15 kV) and low-energy electron flooding for charge compensation. To compensate for surface charge effects, the binding energies were calibrated using the C1*s* hydrocarbon peak at 284.80 eV.

Electron paramagnetic resonance (EPR) spectra at the X-band frequency (≈9.7 GHz) were recorded at room temperature with a Bruker EMX-8 spectrometer. The g factor was calculated by the equation $h\upsilon = g\beta H$, where h is Planck's constant, H is the applied magnetic field (measured with a teslameter), and β is Bohr's magneton.

Raman spectra were obtained in a backscattering configuration on a Renishaw 1000 confocal laser Raman spectrometer with a 25-mW Ar^+ laser (514.5 nm) and a 20× long-focus lens. The time of acquisition was 60 s.

Temperature-programmed reduction with H_2 (H_2-TPR) experiments were performed in a quartz reactor with a thermal conductivity detector (TCD) to monitor the H_2 consumed. A 50-mg sample (10-mg for Fe_2O_3) was pretreated *in situ* at 500 °C for 1 h in a flow of O_2 and cooled to room temperature in the presence of O_2. TPR was conducted at 10 °C/min up to 700 °C in a 30-ml/min flow of 5 vol.% H_2 in N_2. After the first cycle, the sample was cooled to room temperature in the H_2/N_2 mixture. The sample was then reoxidized at 500 °C for 1 h in O_2 and cooled to room temperature in O_2, and then a second TPR run was conducted. Similar consecutive TPR runs were carried out over several cycles. To quantify the total amount of H_2 consumed during these experiments, CuO was used as a calibration reference.

2.3. Reactions

2.3.1. TPO reactions

The TPO reactions were conducted in a fixed-bed micro reactor consisting of a quartz tube (6 mm i.d.). Printex-U from Degussa was used as the model soot. The mixture of soot and catalyst in a weight ratio of 1:9 under tight contact was obtained by grinding the soot with the catalyst in an agate mortar for 30 min and pressing for 10 min at 20 MPa, and then crushing and sieving to 20–60 mesh [20]. For pure soot combustion (noncatalytic), the catalyst was replaced with silica. The tight contact between the soot and the catalyst was confirmed by FESEM (Fig. S1 in the Supplementary Information). Typically, a mixture of 100 mg, diluted with silica to favor heat transfer, is pretreated at 200 °C for 30 min in high-purity He (30 ml/min), and then heated from room temperature to 700 °C at a heating rate of 5 °C/min in a flow of 10 vol.% O_2 + He at a flow rate of 100 ml/min. The outlet concentrations in the product gas were measured online by an SP-6890 gas chromatograph (GC) (Shandong Lunan Ruihong Chemical Instrument Corporation, China) fitted with a methanator. A flame ionization detector (FID) was employed to determine CO and CO_2 concentrations after these gases were separated over a Porapak Q column and converted into methane over a Ni catalyst at 360 °C.

The ignition temperature for soot combustion is evaluated by the value of T_{10}, which is defined as the temperature at which 10% of the soot is converted [21]. The selectivity to CO_2 formation is defined as the CO_2 outlet concentration as a percentage of the sum of the CO_2 and CO outlet concentrations.

2.3.2. Isothermal reactions

Isothermal reactions for soot combustion at 280 °C were conducted, at which a stable and low conversion of soot (<15%) was achieved in an approximate kinetic regime. The selection of 280 °C is made because (1) at 280 °C, the soot conversion is low and (2) at 280 °C, the soot conversion is nearly constant over time (see Fig. 1a). However, lower conversions at lower temperatures were not used in order to obtain accurate enough analyses. Above 280 °C, the soot conversion increases significantly. In this case, the reaction cannot be thought to be in a stable state. Furthermore, a series of experiments were performed to exclude internal and external diffusion and heat transfer. For the pellets of the mixture of catalyst and soot prepared described in Section 2.3.1, we found that there were no intraparticle mass transport limitations when

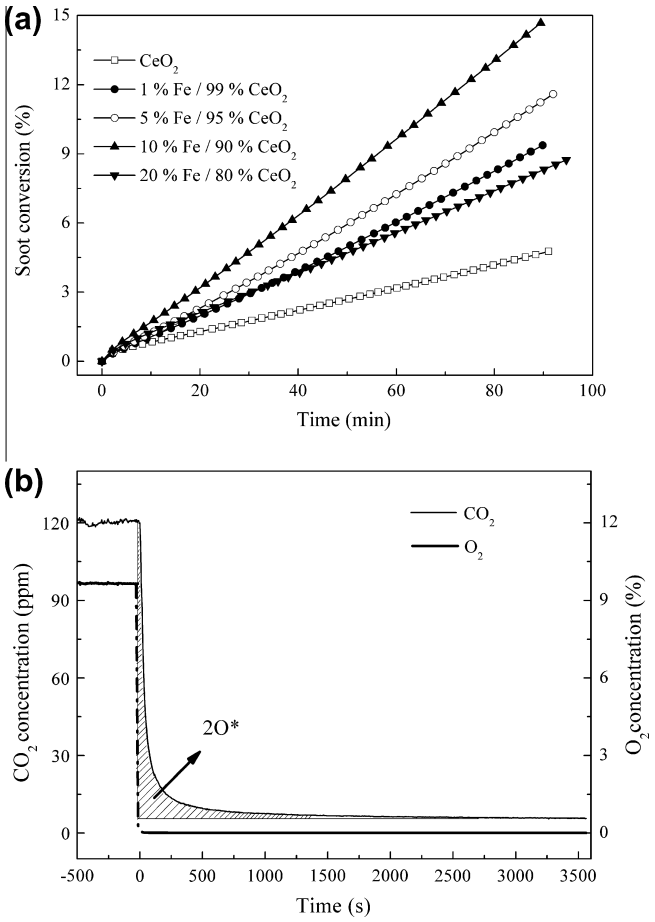

Fig. 1. (a) Soot conversion at 280 °C as a function of time over x%Fe/y%CeO_2 and CeO_2; (b) CO_2 concentrations at 280 °C as a function of time over 10%Fe/90%CeO_2 before and after O_2 is removed from the reactant feed.

the diameter was below 48 μm. For a total flow rate of about 150 ml/min, no external mass transport limitations were detected. When the conversion of soot is lower than 15%, the temperature increase of the diluted catalyst bed is not found. Thus, the reaction rate for soot combustion can be obtained from the slope of the lines, as shown in Fig. 1a. During isothermal anaerobic titrations, soot is regarded as the probe molecule. As shown in Fig. 1b, O_2 is instantaneously removed from the reactant stream and is replaced with a flow of He. The transient decay in concentrations from the steady state was monitored using a quadruple mass spectrometer (MS, OmniStar 200, Balzers) with a m/z of 44 for CO_2 and 32 for O_2. The distance between MS and the reactor is as small as possible (about 1 m). Before experiments, MS was carefully calibrated by standard gas. The number of active redox sites available to soot under these reaction conditions can be quantified by integrating the diminishing rate of CO_2 formation over time (the shaded area),

$$O^* \text{ amount } (\text{mol/g}) : \frac{2FAP_0 \times 10^{-6}}{RTm} \quad (1)$$

$$O^* \text{density } (\text{nm}^{-2}) : \frac{2 \times 6.02FAP_0 \times 10^{-1}}{RTmS}, \quad (2)$$

where A is the shaded area (s), F is the volumetric flow rate (L/s), m is the mass of the catalyst (g), P_0 is the atmospheric pressure (Pa), R is the gas constant, T is room temperature (K), and S is the specific surface area (m^2/g).

3. Results

3.1. Characterization

3.1.1. XRD and TEM

Our detailed XRD results show that the α-Fe_2O_3 phase with a hexagonal haematite structure is detected only when $y \geqslant 30$ (Fig. S2 in the Supplementary Information), in agreement with Ref. [22]. Fig. 2 shows the step scan XRD patterns of the CeO_2 and x%Fe/y%CeO_2 samples after calcination at 650 °C for 6 h. All samples give identical reflections and match what is expected for pure CeO_2 with a cubic fluorite structure (*Fm3m*, JCPDS 34-0394), suggesting a high level of Fe incorporation within CeO_2. The unit cell parameter (a) was thus calculated and is shown in Table 1 with standard deviations. Instead of a decrease in a due to the substitution of the smaller Fe^{3+} ions (the ionic radius of Fe^{3+} in a six-coordination structure and high spin level is 0.64 Å) for the larger Ce^{4+} ions (the ionic radius of Ce^{4+} in a eight-coordination structure is 0.97 Å), we observed a slight increase in a for the 1%Fe/99%CeO_2 and 5%Fe/95%CeO_2 samples compared with pure CeO_2. However, a monotonic decrease is observed from 1%Fe/99%CeO_2 to 20%Fe/80%CeO_2.

TEM was also conducted for 10%Fe/90%CeO_2 (Fig. S3 in the Supplementary Information). The clear lattice fringes give evidence of well-crystallized samples. The average atomic ratio between Fe and Ce analyzed by EDS was almost the same as in the starting materials. This suggests the incorporation of Fe ions into the CeO_2 structure, which is consistent with XRD results.

3.1.2. Surface areas

The BET surface areas of the CeO_2, x%Fe/y%CeO_2, and Fe_2O_3 samples are also listed in Table 1. Pure Fe_2O_3 (18 m^2/g) has a lower surface area than CeO_2. However, after doping with Fe, the surface areas of the x%Fe/y%CeO_2 samples increase compared to that of pure CeO_2. The largest surface area was obtained for 5%Fe/95%CeO_2 [8].

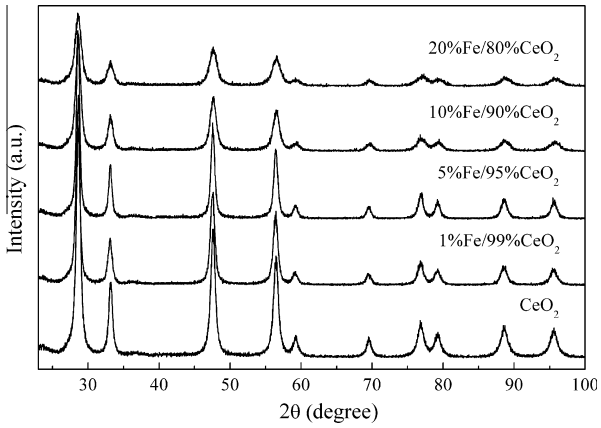

Fig. 2. Step scan XRD patterns of the CeO_2 and x%Fe/y%CeO_2 samples.

Table 1
Textural properties of the CeO_2, x%Fe/y%CeO_2, and Fe_2O_3 samples.

Sample	Unit cell parameter, a (Å)	Crystallite size (nm)	BET surface area (m^2/g)
CeO_2	5.4023 ± 0.0015	14.5	50.6
1%Fe/99%CeO_2	5.4087 ± 0.0009	14.0	62.6
5%Fe/95%CeO_2	5.4046 ± 0.0003	18.5	64.3
10%Fe/90%CeO_2	5.3974 ± 0.0010	11.7	55.6
20%Fe/80%CeO_2	5.3966 ± 0.0007	7.8	53.4
Fe_2O_3	–	–	18.0

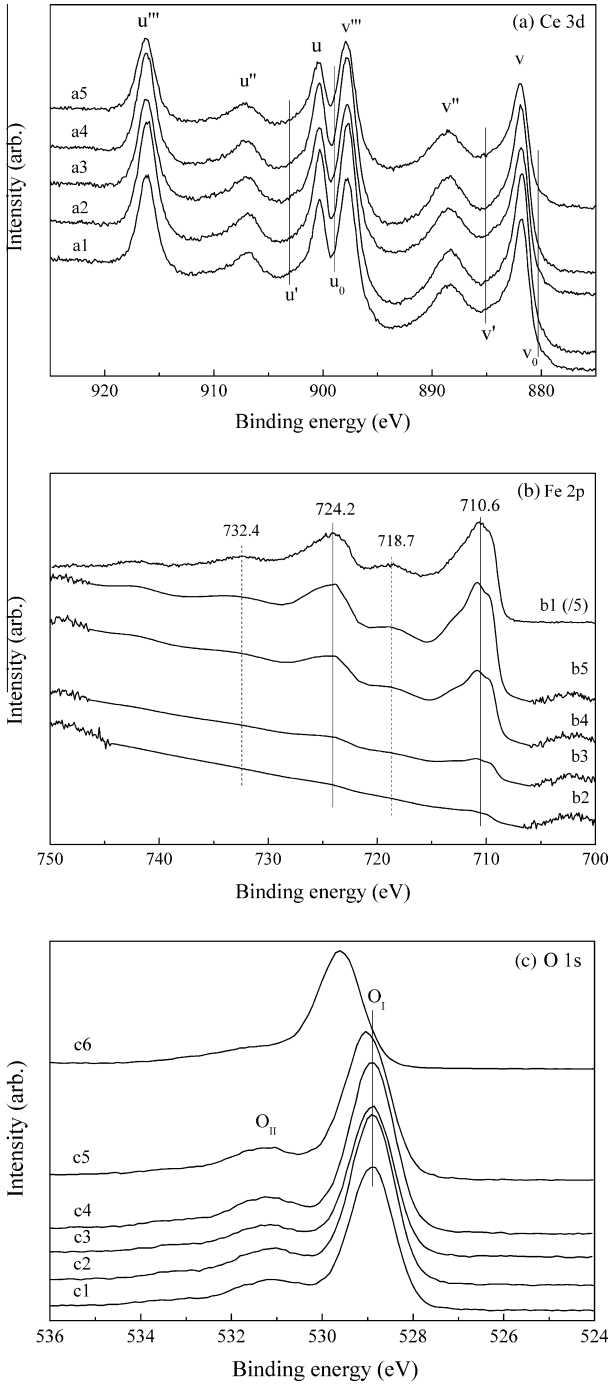

Fig. 3. XPS spectra of Ce3*d* (a), Fe2*p* (b), and O1*s* (c) for CeO_2, *x*%Fe/*y*%CeO_2, and Fe_2O_3. (a1, c1) CeO_2; (b1, c6) Fe_2O_3; (a2, b2, and c2) 1%Fe/99%CeO_2; (a3, b3, and c3) 5%Fe/10%CeO_2; (a4, b4, and c4) 10%Fe/90%CeO_2; (a5, b5, and c5) 20%Fe/80%CeO_2.

3.1.3. XPS

Fig. 3 shows the Ce3*d* (a), Fe2*p* (b), and O1*s* (c) spectra of CeO_2, *x*%Fe/*y*%CeO_2, and Fe_2O_3. In the Ce3*d* spectra, the peaks labeled *u* and *v* refer to the $3d_{3/2}$ and $3d_{5/2}$ spin–orbit components, respectively. The dominant peaks denoted by *v*, *v*″, *v*‴, *u*, *u*″, and *u*‴ are characteristic peaks of Ce^{4+} ions, whereas those marked by v_0, *v*′, u_0, and *u*′ are of Ce^{3+} ions, which can only be slightly distinguished. This suggests that the Ce seems to be mostly in a +4 oxidation state [23]. The Fe2*p* spectra show characteristic Fe2$p_{3/2}$ and Fe2$p_{1/2}$ peaks at binding energies of 710.6 and 724.2 eV, respectively [24]. Two weak satellite peaks at 718.7 and 732.4 eV were also distinguished. This indicates that Fe is in a +3 oxidation state. The surface atomic ratios of Fe/Ce for *x*%Fe/*y*%CeO_2 are summarized in Table 2. Each value was higher than that of the bulk (stoichiometry). Although solid solutions were formed for the *x*%Fe/*y*%CeO_2 samples, an enrichment of Fe on the surface was detected.

In the O1*s* spectra (Fig. 3c), a significant peak was observed for Fe_2O_3, which can be assigned to lattice oxygen. However, a main peak (O_I) and a shoulder (O_{II}) were detected for CeO_2 and *x*%Fe/*y*%CeO_2. Generally, the former corresponds to bulk oxygen, while the later represents various surface oxygen species. It is observed that the O_I peak shifts to higher energy for 20%Fe/80%CeO_2, possibly due to the presence of FeO_x aggregates on the surface. As given in Table 2, the surface atomic ratios of O/(Ce + Fe) for *x*%Fe/*y*%CeO_2 were lower than those of the stoichiometry (2.0), suggesting the existence of O vacancies on these sample surfaces.

Table 2
The atomic ratios of Fe/Ce and O/(Ce + Fe) by XPS surface compositional analysis.

Sample	Fe/Ce	O/(Ce + Fe)	Stoichiometric Fe/Ce
1%Fe/99%CeO_2	0.015	1.969	0.010
5%Fe/95%CeO_2	0.058	1.739	0.053
10%Fe/90%CeO_2	0.156	1.926	0.111
20%Fe/80%CeO_2	0.350	1.871	0.250

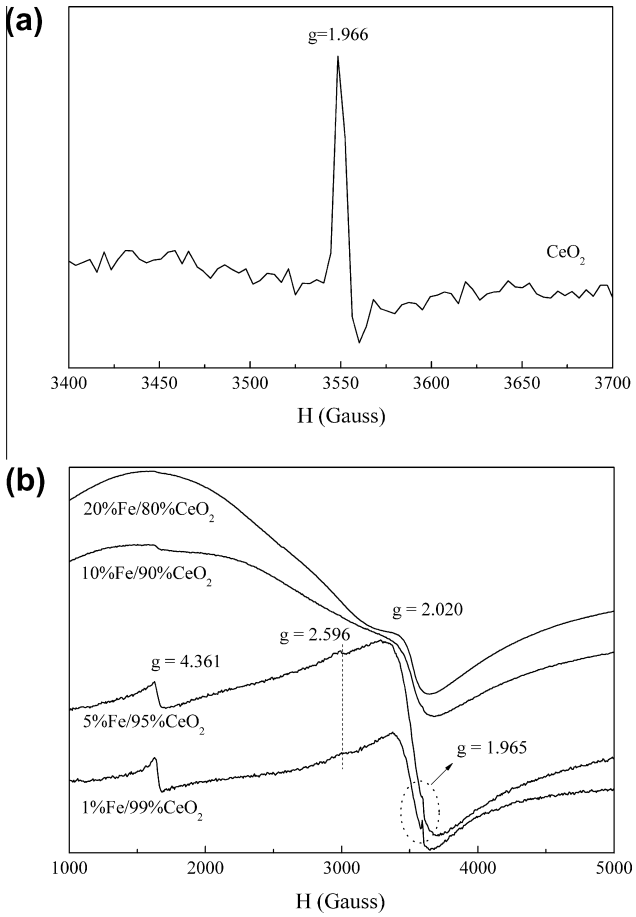

Fig. 4. EPR spectra of CeO_2 (a) and *x*%Fe/*y*%CeO_2 (b) at room temperature.

3.1.4. EPR

Fig. 4 shows the EPR spectra of CeO_2 (a) and *x*%Fe/*y*%CeO_2 (b) at room temperature. The characteristic signal of Ce^{3+} was observed at *g* = 1.966 for CeO_2 (Fig. 4a) [25]. Similarly to that reported in

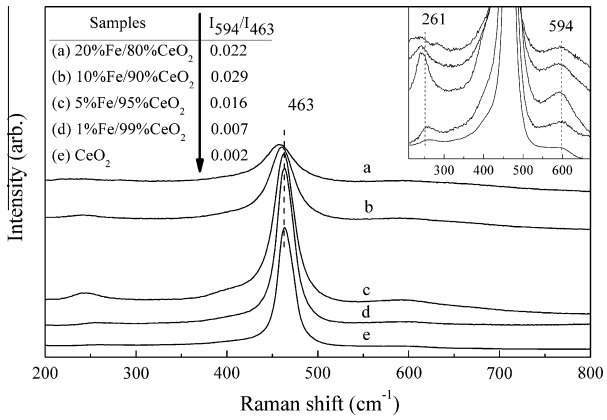

Fig. 5. Raman spectra of the x%Fe/y%CeO_2 samples.

[26], the oxygen vacancy signals for O_2^- and O^- cannot be distinguished at room temperature because of their low relaxation spin times [27]. For x%Fe/y%CeO_2, each spectrum is a superposition of the signals from Ce^{3+} and Fe^{3+} ions. As shown in Fig. 4b, the two EPR signals centered at $g = 2.020$ and $g = 4.361$ are associated with the Fe^{3+}–O_6 unit having a distorted rhombic symmetry [28]. Furthermore, a new weak signal at $g = 2.596$ appeared for 1%Fe/99%CeO_2 and 5%Fe/95%CeO_2, which can be attributed to the formation of the Fe–O–Ce bond [28–30]. It is observed that the incorporation of low-valence ions, such as Sr^{2+} (La^{3+}or Y^{3+}), into the Ce–Zr–O mixed oxides would result in the presence of a new type of paramagnetic centers in EPR spectra due to the formation of Ce–O–Sr (La or Y) bonds [29 and references therein]. The strong interaction between Fe and Ce ions with a partial transfer of unpaired electron density from Ce^{3+} to Fe^{3+} (Fe is more electronegative than Ce) induces the g-value variation [30]. The broad resonance linewidth of the $g = 2.020$ signal for 10%Fe/90%CeO_2 and 20%Fe/80%CeO_2 indicates the formation of Fe–O clusters on the surface and the strong magnetic dipole interactions among these fine clusters, which also shields the signals of Ce^{3+} and Fe–O–Ce, as observed for 1%Fe/99%CeO_2 and 5%Fe/95%CeO_2. In addition, the disappearance of the $g = 4.361$ signal for 20%Fe/80%CeO_2 suggests the complete formation of FeO_x aggregates [31].

3.1.5. Raman

Fig. 5 shows the Raman spectra of the x%Fe/y%CeO_2 and CeO_2 samples. The intense band observed at ~463 cm^{-1} can be assigned to the symmetric breathing mode of the O atoms around each Ce^{4+} because that is the only allowed Raman mode with F_{2g} symmetry in metal oxides with a fluoride structure [32], and this coincides with our XPS results. The peak shifts toward a lower frequency and becomes progressively broader and asymmetric with an increase in the doping content, which can be explained by lattice distortions due to the incorporation of Fe into CeO_2 [33]. Two weak second-order peaks appear at 261 cm^{-1} and 594 cm^{-1}, which are characteristic of a transverse acoustic mode and oxygen vacancies in the ceria lattice, respectively, as clearly seen in the inset [34]. The Raman spectrum for Fe_2O_3 exhibits four bands at 222, 288, 407, and 605 cm^{-1}, respectively, which are not observed at all in Fig. 5. One reason for this is that the Raman bands in Fe_2O_3 are much weaker than those in CeO_2 due to the strong absorbance of haematite at the wavenumber region of the Raman spectrum. The other is related to the formation of Ce–Fe solid solutions [8].

Importantly, as shown by the I_{594}/I_{463} values, the oxygen vacancy concentration reaches a maximum for 10%Fe/90%CeO_2. This phenomenon has been explained in the literature [8]. Fe^{3+} prefers to occupy the substituted Ce^{4+} sites in the ceria structure (1%Fe/99%CeO_2 and 5%Fe/95%CeO_2), and thus the oxygen vacancy concentrations increase as the amount of doped Fe^{3+} increases, but when the amount of doped Fe^{3+} exceeds a critical value (10%Fe/90%CeO_2), Fe^{3+} gradually becomes interstitial within the ceria structure, which would decrease the oxygen vacancy concentrations (20%Fe/80%CeO_2).

The presence of oxygen vacancies and the corresponding Ce^{3+} can be used to explain the change in cell parameters of the x%Fe/y%CeO_2 samples, which is observed in the XRD results. Because of the smaller Ce^{4+} ion (0.97 Å) compared with the Ce^{3+} ion (1.23 Å), the slight unit cell expansion for the 1%Fe/99%CeO_2 and 5%Fe/95%CeO_2 samples can be attributed to the partial reduction of Ce^{4+} to Ce^{3+} [35]. Nevertheless, with an increase in the amount of Fe^{3+} (0.64 Å), a gradual shrinkage of the unit cell is expected. The combination of these two factors results in a smaller cell parameter for 10%Fe/90%CeO_2 compared with CeO_2 irrespective of its having the highest concentration of oxygen vacancies. A further decrease in a is certain for 20%Fe/80%CeO_2 because of the decrease in oxygen vacancy concentration and a simultaneous increase in the amount of Fe.

3.1.6. H_2-TPR

Fig. 6 shows the H_2-TPR profiles of the Fe_2O_3, CeO_2, and x%Fe/y%CeO_2 samples during the fourth cycle (the first cycle for Fe_2O_3). The cyclic TPR profile characteristics were almost reproducible after the first cycle (Fig. S4 in the Supplementary Information), indicating that the redox reaction is reversible. Therefore, as an example, the fourth TPR spectra are discussed below. Fe_2O_3 shows

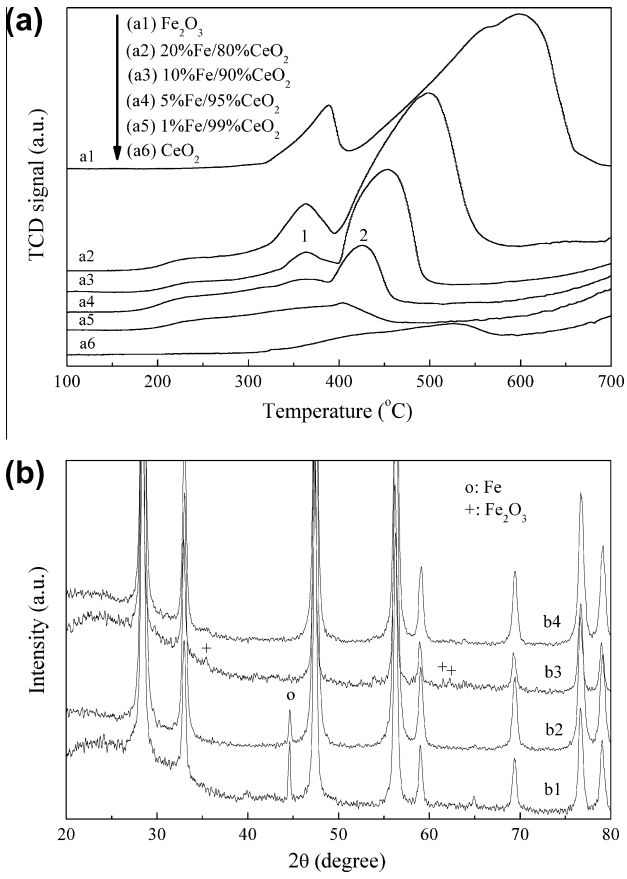

Fig. 6. (a) H_2-TPR profiles of the x%Fe/y%CeO_2 samples during the fourth cycle (the first cycle for Fe_2O_3); (b) XRD patterns of 20%Fe/80%CeO_2 after four cycles of H_2-TPR (b1); 10%Fe/90%CeO_2 after four cycles of H_2-TPR (b2); 20%Fe/80%CeO_2 after four cycles of H_2-TPR and reoxidation by O_2 (b3); 10%Fe/90%CeO_2 after four cycles of H_2-TPR and reoxidation by O_2 (b4).

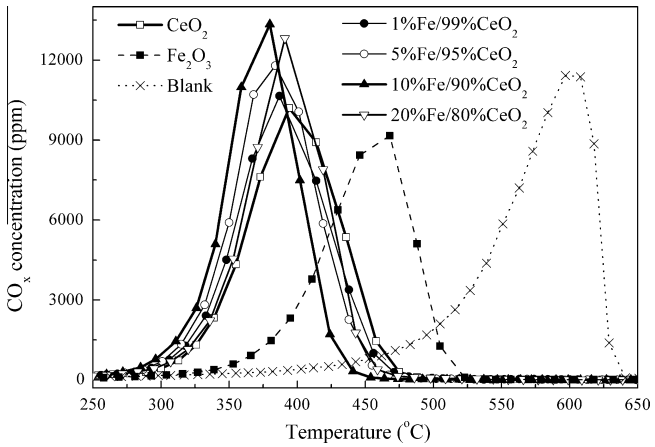

Fig. 7. TPO patterns of CO_x for soot combustion with O_2 over the x%Fe/y%CeO_2, CeO_2, and Fe_2O_3 samples under a tight contact condition between soot and catalyst.

a sharp peak at 385 °C and a strong peak at 590 °C, corresponding to the reduction of haematite to magnetite (Fe_3O_4) and of magnetite to Fe^0 (Fig. 6b), respectively [36]. CeO_2 shows a characteristic profile for ceria reduction with a broad peak from about 325 °C [37]. 1%Fe/99%CeO_2 shows behavior similar to that of CeO_2; however, the reduction temperature is considerably lower than that of CeO_2, suggesting that the incorporation of Fe increases the mobility of the surface lattice oxygen. In contrast, the 5%Fe/95%CeO_2, 10%Fe/90%CeO_2, and 20%Fe/80%CeO_2 samples show two peaks. Peak 1 does not show distinguishable temperature differences, which means that the reducibility of these three samples is comparable. However, the intensities of Peak 1 and Peak 2 increase as the amount of Fe increases, suggesting that they are related to the reduction of the Fe species. Furthermore, Peak 2 only appears after the first TPR cycle (Fig. S4 in the Supplementary Information) and shifts to higher temperatures with an increase in the amount of Fe, revealing that Fe segregates to the surface from the bulk after the first redox reaction. At higher levels of Fe doping, the segregation is more serious. As shown in Fig. 6b, Fe^0 was observed for 20%Fe/80%CeO_2 and 10%Fe/90%CeO_2 after the fourth cycle of H_2-TPR. This means that the reduction process is accompanied by metal particle agglomeration. After four cycles of H_2-TPR and reoxidation by O_2, XRD patterns for 20%Fe/80%CeO_2 and 10%Fe/90%CeO_2 were obtained and are also shown in Fig. 6b. 20%Fe/80%CeO_2 consists of a bulk Fe_2O_3 phase. A quantitative analysis (see the Supplementary Information) shows that approximately 15 at.% Fe ($x = 15$) is segregated as bulk Fe_2O_3 to the surface of 20%Fe/80%CeO_2 and, therefore, only 5 at.% Fe ($x = 5$) is redispersed over/within the CeO_2 crystallites. Actually, the bulklike FeO_x aggregates for the fresh 20%Fe/80%CeO_2 sample were already distinguished by the presence of a weak Peak 2 in the first TPR spectra (Supplementary Information), in agreement with the XPS and EPR analysis. However, 10%Fe/90%CeO_2 does not show a bulk Fe_2O_3 phase, suggesting that all the Fe^0 is reoxidized into Fe_2O_3 and redispersed over the CeO_2 crystallites as extremely small Fe–O clusters in proximity to Ce or directly incorporated within the CeO_2 lattice to form solid solutions. This is also the case for 1%Fe/99%CeO_2 and 5%Fe/95%CeO_2. Consequently, the TPR process is reproducible after the first cycle for all x%Fe/y%CeO_2 samples. Because the reduction temperatures (Peak 1) are much lower than those of pure CeO_2 and Fe_2O_3, the presence of a strong interaction between Fe and Ce is expected, which may be attributed to the reduction of surface Fe–O–Ce species (neither bulk Fe_2O_3 nor bulk CeO_2). This is called synergism due to the high dispersion of Fe ions over the CeO_2 surface or the formation of the Ce–Fe solid solution [38]. From the discussions above, the emergence of Peak 2 after the first TPR can easily be attributed to the reduction of the segregated FeO_x species.

Table 3
Ignition temperature and selectivity to CO_2 for soot combustion under tight contact conditions.

Sample	T_{10} (°C)	Selectivity to CO_2 (%)
Blank (noncatalytic)	475	51
CeO_2	343	96
1%Fe/99%CeO_2	335	100
5%Fe/95%CeO_2	334	100
10%Fe/90%CeO_2	328	100
20%Fe/80%CeO_2	340	100
Fe_2O_3	385	99

3.2. Reactions

3.2.1. TPO reactions

Fig. 7 shows the TPO patterns of soot combustion on the x%Fe/y%CeO_2, CeO_2, and Fe_2O_3 samples. T_{10} and CO_2 selectivity for all the samples are summarized in Table 3. The carbon mass balance is between 90 and 100%. Fe_2O_3 decreases T_{10} from 475 °C for noncatalytic combustion to 385 °C; however, its ignition temperature is much higher than that of CeO_2. The x%Fe/y%CeO_2 samples show lower ignition temperatures than pure CeO_2 and Fe_2O_3. The lowest T_{10} was found for 10%Fe/90%CeO_2. T_{10} decreases according to the sequence $Fe_2O_3 \gg CeO_2 >$ 20%Fe/80%$CeO_2 >$ 1%Fe/99%$CeO_2 >$ 5%Fe/95%$CeO_2 >$ 10%Fe/90%CeO_2. Regarding the selectivity toward CO_2 formation, the noncatalytic combustion is only 51%, while all the samples studied had far higher values. Although CeO_2 shows 95% CO_2 selectivity, the x%Fe/y%CeO_2 samples yield nearly 100% CO_2.

3.2.2. Isothermal reactions

Table 4 summarizes the quantified values of the specific reaction rate per BET surface area, the density of active oxygen (O^*), and the TOF for soot combustion with O_2 at 280 °C on the x%Fe/y%CeO_2 and CeO_2 samples. According to the reaction rates, the activity sequence is the same as that for the decrease of T_{10} in the TPO reactions. However, if we consider the effects of surface areas, that is, the specific rate per BET surface area (defined as apparent activity), the sequence 10%Fe/90%$CeO_2 >$ 5%Fe/95%$CeO_2 \approx$ 20%Fe/80%$CeO_2 >$ 1%Fe/99%$CeO_2 > CeO_2$ is observed. 20%Fe/80%CeO_2 is more active than 1%Fe/99%CeO_2. On the other hand, if we consider the rate per O^* site, namely TOF (intrinsic activity), the sequence 10%Fe/90%$CeO_2 \approx$ 5%Fe/95%$CeO_2 \approx$ 20%Fe/80%$CeO_2 >$ 1%Fe/99%$CeO_2 > CeO_2$ is observed. The similar TOF values imply that the active sites have the same activity, and larger TOF values indicate that the sites are more active.

In order to check the validity of the method, another 10%Fe/90%CeO_2 sample was prepared using the same procedure. Isothermal reactions were performed in tight contact between soot and catalyst with the mass ratios of 1:9, 1:6, and 1:12. The O^* density was 0.68, 0.70, and 0.67, respectively, which are close to 0.62 (Table 4). This suggests that the proposed method is reproducible and authentic. Furthermore, a limited change in the ratios between soot and catalyst has little effects on the results.

4. Discussion

Although the fresh x%Fe/y%CeO_2 samples formed CeO_2 solid solutions, the characterization results show that Fe is highly segregated to the surface of x%Fe/y%CeO_2 after the redox reactions. This suggests that Fe plays an important role in soot combustion. However, the bulk Fe_2O_3 (Fe–O–Fe) on the catalyst surface is evidently

Table 4
Reaction rate, active oxygen (O^*) density, and TOF of the O^* site for soot combustion with O_2 at 280 °C over the CeO_2 and x%Fe/y%CeO_2 samples under tight contact conditions.

Sample	Rate (mol s^{-1} g^{-1} × 10^{-7})	Specific rate (mol s^{-1} m^{-2} × 10^{-9})	O^* amount (mol g^{-1} × 10^{-5})	O^* density (O^* nm^{-2})	TOF (s^{-1} × 10^{-3})
CeO_2	0.71	1.40	2.55	0.30	2.78
1%Fe/99%CeO_2	1.41	2.25	4.13	0.40	3.41
5%Fe/95%CeO_2	1.66	2.58	4.36	0.41	3.81
10%Fe/90%CeO_2	2.20	3.96	5.72	0.62	3.85
20%Fe/80%CeO_2	1.35	2.52	3.45	0.39	3.90

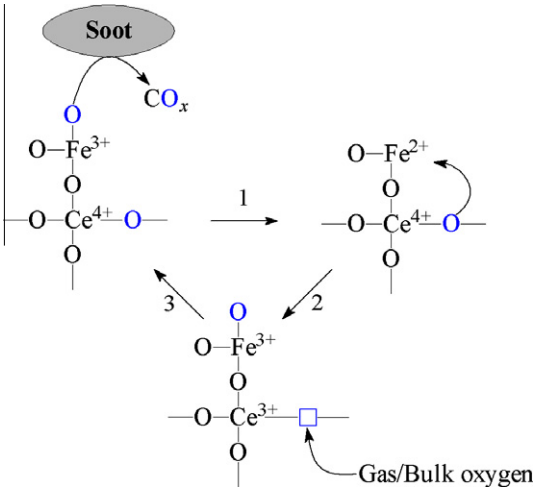

Fig. 8. Mechanism of soot combustion with O_2 over the x%Fe/y%CeO_2 catalysts.

not the active phase in the temperature range of soot combustion, as shown by TPO results. Fe_2O_3 has been shown to have a "push–pull" redox mechanism for soot combustion at higher temperatures [5]. Only the surface or subsurface layers of the iron oxide participate in the oxygen transfer. Reoxidation by neighboring oxygen leads to a cascade of formation and refilling of surface oxygen vacancies. Therefore, Fe_2O_3 is not as reactive as CeO_2.

As shown in Fig. 1b, irrespective of the fact that no oxygen was fed to the reactor, and a relatively high feed flow rate (150 ml/min), and low mass of catalyst (45 mg) and low reaction temperature (280 °C) were used, the CO_2 signal decreased slowly. The physisorbed oxygen, chemisorbed oxygen, and bulk oxygen are involved in the anaerobic soot combustion reaction [39]. This is reasonable considering the OSC of CeO_2. Raman results prove the existence of oxygen vacancies. The mobility of oxygen ions via oxygen vacancies occurs readily, which suggests that the redox cycles between Ce^{4+} and Ce^{3+} can promote the reactivity of Fe_2O_3, as shown by the fact that the TPR peaks for x%Fe/y%CeO_2 are lower than those of Fe_2O_3.

As indicated above, the x%Fe/y%CeO_2 and CeO_2 samples show that the temperature of H_2 reduction (Peak 1) has the sequence 10%Fe/90%CeO_2 ≈ 5%Fe/95%CeO_2 ≈ 20%Fe/80%CeO_2 < 1%Fe/99%CeO_2 < CeO_2, which is correlated to that of the TOF values. This suggests that soot oxidation proceeds through a redox mechanism. As discussed above, two kinds of active sites, Fe–O–Ce (Fe–O species in proximity to Ce on the surface or within the CeO_2 lattice) and Ce–O–Ce, are involved in soot combustion. Evidently, the former are responsible for the activity of 10%Fe/90%CeO_2, 5%Fe/95%CeO_2, and 20%Fe/80%CeO_2, and the latter for CeO_2. Both sites might be contained within 1%Fe/99%CeO_2, considering that the amount of Fe doping is too low to form enough Fe–O–Ce species. Because the TOF value for Fe–O–Ce is much higher than that for Ce–O–Ce, the enhanced reactivity of CeO_2 should be attributed to the redox cycle between Fe^{3+} and Fe^{2+}.

According to the above-mentioned bifunctional promoted effects between Fe and Ce, the reactive mechanism of the Fe–O–Ce species is schematically described in Fig. 8 using a redox cycle. First, the surface oxide anion bound to Fe^{3+} reacts with soot at the soot/catalyst interface to give out CO_x with the production of oxygen vacancies, and reduced-state Fe^{2+} is obtained (Path 1). The Ce^{4+} cation at the neighboring site of the reduced Fe^{2+} site can supply additional oxygen atoms from the catalyst lattice through the reduction of Ce^{4+} to Ce^{3+}, while Fe^{2+} is simultaneously oxidized to Fe^{3+} (Path 2). Another surface-active oxygen species is thus formed, on which the next combustion reaction takes place. Ce^{3+} (with oxygen vacancies) may be reoxidized directly by gas phase oxygen or by oxygen diffusion through the bulk of the catalyst (Path 3).

The assignment of active sites above can be used to explain the different soot combustion behavior among varieties of x%Fe/y%CeO_2. The maximum apparent activity for 10%Fe/90%CeO_2 is due solely to its having the highest O^* density, corresponding to the maximum oxygen vacancy concentrations, which originates from the high Fe content. However, to explain why the apparent activity for 20%Fe/80%CeO_2 does not increase with an increase in Fe content compared to 10%Fe/90%CeO_2, it needs to be considered that only about 5 at.% Fe is redispersed over/within the CeO_2 to form Fe–O–Ce species for 20%Fe/80%CeO_2. This results in the same O^* density as for 5%Fe/95%CeO_2, and thus the apparent activity for 20%Fe/80%CeO_2 is nearly equal to that of 5%Fe/95%CeO_2. Aneggi et al. [6] pointed out that the segregation of Fe on the surface as bulk Fe_2O_3 is the main cause of degradation of activity for the Fe-doped CeO_2. We confirm this result from the viewpoint of active sites. Furthermore, we find a similar O^* density among 1%Fe/99%CeO_2, 5%Fe/95%CeO_2, and 20%Fe/80%CeO_2, as listed in Table 3, but the TOF value of 1%Fe/99%CeO_2 is less than that of 5%Fe/95%CeO_2 (20%Fe/80%CeO_2). The reason for this is that both the Fe–O–Ce and Ce–O–Ce sites are active in 1%Fe/99%CeO_2. Therefore, the apparent activity for 1%Fe/99%CeO_2 is lower than that of 5%Fe/95%CeO_2 (20%Fe/80%CeO_2) but higher than that of CeO_2.

We would also like to point out that Fe_2O_3 [40] and CeO_2–Fe_2O_3 mixed oxides [8] are very effective catalysts for CO oxidation. Normally, trivalent metal dopants improve the selectivity of CeO_2 toward CO_2 formation [41]. Therefore, it is easy to comprehend the especially high CO_2 selectivity in this work.

5. Conclusions

From the results of XRD, XPS, N_2 adsorption/desorption, Raman, EPR, H_2-TPR, FT-IR, measurements of active sites, and TOF, the following conclusions are made.

Fe-doped CeO_2 for soot catalytic combustion (oxidation) with O_2 yields activity higher than that of pure CeO_2 and Fe_2O_3. The optimum Fe content is Fe/(Ce + Fe) = 10 at.% according to soot ignition temperatures. However, on the basis of turnover frequencies, the samples with a Fe/(Ce + Fe) ratio within 5–20 at.% show similar activity.

The reaction proceeds through a redox cycle between Ce^{4+}/Fe^{3+} and Ce^{3+}/Fe^{2+}. The active sites are composed of the Fe–O–Ce

species, which can be accurately quantified by isothermal anaerobic titration with soot as a probe molecule.

The methodology for quantifying the active redox site densities and turnover frequencies is crucial for the comparison of activity for catalysts of different compositions and produced by different synthesis methods. Determination of the reaction mechanism is thus highly reliable, and this method can be extended to soot combustion on all similar oxides that react through a redox process that includes lattice oxygen.

Acknowledgments

This work was supported by the 863 program of the Ministry of Science and Technology of the People's Republic of China (No. 2008AA06Z320), the National Natural Science Foundation of China (No. 20777028), the Natural Science Foundation of Shandong Province (No. Y2007B36), and the Program of the Development of Science and Technology of Shandong Province (No. 2008GG10003026). The authors acknowledge Xin Li for H_2-TPR measurements and Dr. Zhongpeng Wang for checking the English writing.

Appendix A. Supplementary material

Supplementary data associated with this article can be found, in the online version, at doi:10.1016/j.jcat.2010.08.017.

References

[1] A. Setiabudi, J. Chen, G. Mul, M. Makkee, J.A. Moulijn, Appl. Catal. B 51 (2004) 9.
[2] M.S. Gross, M.A. Ulla, C.A. Querini, Appl. Catal. A 360 (2009) 81.
[3] T. Campenon, P. Wouters, G. Blanchard, P. Macaudiere, T. Seguelong, SAE Technical Paper, p. 2004-01-0071.
[4] V. Harle, C. Pitois, L. Rocher, F. Garcia, SAE Technical Paper, p. 2008-01-0331.
[5] D. Reichert, H. Bockhorn, S. Kureti, Appl. Catal. B 80 (2008) 248.
[6] E. Aneggi, C. de Leitenburg, G. Dolcetti, A. Trovarelli, Catal. Today 114 (2006) 40.
[7] D. Yan, H. Wang, K. Li, Y. Wei, X. Zhu, X. Cheng, Acta Phys. Chim. Sin. 26 (2010) 331.
[8] H. Bao, X. Chen, J. Fang, Z. Jiang, W. Huang, Catal. Lett. 125 (2008) 160.
[9] P. Singh, M.S. Hegde, J. Solid State Chem. 181 (2008) 3248.
[10] P. Darcy, P. Da Costa, H. Mellottée, J.-M. Trichard, G. Djéga-Mariadassou, Catal. Today 119 (2007) 252.
[11] M. Boudart, Chem. Rev. 95 (1995) 661.
[12] S.E. Siporin, R.J. Davis, J. Catal. 225 (2004) 359.
[13] M. Kuriyama, H. Tanaka, S. Ito, T. Kubota, T. Miyao, S. Naito, K. Tomishige, K. Kunimori, J. Catal. 252 (2007) 39.
[14] K. Suzuki, Y. Aoyagi, N. Katada, M. Choi, R. Ryoo, M. Niwa, Catal. Today 132 (2008) 38.
[15] Z. Zhu, G. Lu, R.T. Yang, J. Catal. 192 (2000) 77.
[16] H. Tian, E.I. Ross, I.E. Wachs, J. Phys. Chem. B 110 (2006) 9593.
[17] Z. Zhang, Y. Zhang, Z. Wang, X. Gao, J. Catal. 271 (2010) 12.
[18] H. Nair, C.D. Baertsch, J. Catal. 258 (2008) 1.
[19] C.S. Polster, H. Nair, C.D. Baertsch, J. Catal. 266 (2009) 308.
[20] B. van Setten, M. Makkee, J.A. Moulijn, Catal. Rev. Sci. Eng. 43 (2001) 489.
[21] J. Oi-Uchisawa, S. Wang, T. Nanba, A. Ohi, A. Obuchi, Appl. Catal. B 44 (2003) 207.
[22] H. Kaneko, H. Ishihara, S. Taku, Y. Naganuma, N. Hasegawa, Y. Tamaura, J. Mater. Sci. 43 (2008) 3153.
[23] E. Bêche, P. Charvin, D. Perarnau, S. Abanades, G. Flamant, Surf. Interface Anal. 40 (2008) 264.
[24] C.F. Petre, F. Larachi, AIChE J. 53 (2007) 2170.
[25] N. Sergent, J.-F. Lamonier, A. Aboukais, Chem. Mater. 12 (2000) 3830.
[26] M. Zhao, M. Shen, J. Wang, J. Catal. 248 (2007) 258.
[27] C. Oliva, G. Termignone, F.P. Vatti, L. Forni, A.V. Vishniakov, J. Mater. Sci. 31 (1996) 6333.
[28] L. Li, G. Li, R.L. Smith, H. Inomata, Chem. Mater. 12 (2000) 3705.
[29] M. Zhao, M. Shen, X. Wen, J. Wang, J. Alloys Compd. 457 (2008) 578.
[30] E.V. Frolova, M. Ivanovskaya, V. Sadykov, G. Alikina, A. Lukashevich, S. Neophytides, Prog. Solid State Chem. 33 (2005) 317.
[31] A. Gervasini, C. Messi, A. Ponti, S. Cenedese, N. Ravasio, J. Phys. Chem. C 112 (2008) 4635.
[32] J.R. McBride, K.C. Hass, B.D. Poindexter, W.H. Weber, J. Appl. Phys. 76 (1994) 2435.
[33] G. Li, R.L. Smith, H. Inomata, J. Am. Chem. Soc. 123 (2001) 11091.
[34] Z. Li, L. Li, Q. Yuan, W. Feng, J. Xu, L. Sun, W. Song, C. Yan, J. Phys. Chem. C 112 (2008) 18405.
[35] A. Gupta, A. Kumar, U.V. Waghmare, M.S. Hegde, Chem. Mater. 21 (2009) 4880.
[36] F.J. Perez-Alonso, I. Melián-Cabrera, M. López Granados, F. Kapteijn, J.L.G. Fierro, J. Catal. 239 (2006) 340.
[37] G. Neri, A. Pistone, C. Milone, S. Galvagno, Appl. Catal. B 38 (2002) 321.
[38] A. Pintar, J. Batista, S. Hočevar, J. Colloid Interface Sci. 285 (2005) 218.
[39] G. Sedmak, S. Hocevar, J. Levec, J. Catal. 213 (2003) 135.
[40] S. Wagloehner, D. Reichert, D. Leon-Sorzano, P. Balle, B. Geiger, S. Kureti, J. Catal. 260 (2008) 305.
[41] A. Bueno-López, K. Krishna, M. Makkee, J.A. Moulijn, J. Catal. 230 (2005) 237.